



CHALMERS
UNIVERSITY OF TECHNOLOGY

On the structural and magnetic properties of the double perovskite Nd₂NiMnO₆Nd₂NiMnO₆

Downloaded from: <https://research.chalmers.se>, 2023-05-04 22:25 UTC

Citation for the original published paper (version of record):

Cedervall, J., Ivanov, S., Lewin, E. et al (2019). On the structural and magnetic properties of the double perovskite Nd₂NiMnO₆Nd₂NiMnO₆. Journal of Materials Science: Materials in Electronics, 30(17): 16571-16578. <http://dx.doi.org/10.1007/s10854-019-02035-z>

N.B. When citing this work, cite the original published paper.



On the structural and magnetic properties of the double perovskite $\text{Nd}_2\text{NiMnO}_6$

Johan Cedervall¹ · Sergey A. Ivanov^{2,3} · Erik Lewin¹ · Premysl Beran^{4,5} · Mikael S. Andersson^{3,6} · Tom Faske⁷ · Gennadii V. Bazuev⁸ · Per Nordblad³ · Martin Sahlberg¹ · Roland Mathieu³

Received: 24 April 2019 / Accepted: 13 August 2019 / Published online: 29 August 2019
© The Author(s) 2019

Abstract

The structural, electronic and magnetic properties of phase pure and stoichiometric samples of the double perovskite $\text{Nd}_2\text{NiMnO}_6$ have been investigated with a combination of X-ray and neutron diffraction, X-ray photoelectron spectroscopy and magnetometry. It is found that the monoclinic space group $P2_1/n$ best describes the crystal structure of $\text{Nd}_2\text{NiMnO}_6$. Photoelectron spectroscopy reveals a mixed valence of the transition metal sites where Ni has 3+/2+ oxidation states and Mn has 3+/4+. The compound orders ferromagnetically at ~195 K. The magnetic structure was determined from the refinement of the neutron diffraction data. The results suggests that the *B*-site magnetic moments align along the crystallographic *a*-direction.

1 Introduction

Rare-earth double perovskite-type materials with general formula $\text{Ln}_2\text{B}'\text{B}''\text{O}_6$ (*Ln*—lanthanide, *B'* and *B''*—3*d* transition metal ions) exhibit a variety of multifunctional properties. Recently research on this class of materials has

increased due to the observation of numerous application-oriented phenomena, such as: magnetocaloric effect [1], magnetoelectric coupling [2], magnetocapacitance and magnetoresistance [3]. These perovskites are rare examples of single material platforms with multiple functions, in which the spins, electric charges, and dipoles can be tuned by magnetic and/or electric fields [2, 3]. Among the ternary transition-metal oxides, La perovskite ferromagnets with mixed-valency of Mn^{3+} and Mn^{4+} has received most attention due to ferromagnetic interaction causing a relatively high Curie temperatures (T_C) reaching 290 K [1–3]. The existence of interesting magnetic properties has stimulated research on other Ln ferromagnetic oxides with Mn in a mixed valency state. The properties of these double perovskites change considerably when La^{3+} is replaced by a rare-earth element with smaller ionic radius (e.g. Nd^{3+}) owing to the change in $\langle \text{Mn}-\text{O}-\text{Ni} \rangle$ bond angles, which causes a decrease of the superexchange interaction strength. As a result, the magnetic transition temperature monotonically decreases with decreasing lanthanide ionic radius [4].

Two magnetic transitions have been reported to occur in $\text{Nd}_2\text{NiMnO}_6$ (NNMO) [5, 6]. A high temperature ferromagnetic transition and a magnetic anomaly at lower temperatures interpreted to indicate a magnetic phase transition. The low-temperature transition has been discussed to originate from $\text{Ni}^{3+} - \text{O} - \text{Mn}^{3+}$ super-exchange interactions, where low-spin Ni^{3+} and high-spin Mn^{3+} are both Jahn-Teller ions [7]. However, super-exchange interactions between ordered Ni^{2+} and Mn^{4+} cations are the likely origin

Electronic supplementary material The online version of this article (doi:<https://doi.org/10.1007/s10854-019-02035-z>) contains supplementary material, which is available to authorized users.

✉ Johan Cedervall
johan.cedervall@kemi.uu.se

¹ Department of Chemistry - Ångström Laboratory, Uppsala University, Box 538, 751 21 Uppsala, Sweden

² Center of Materials Science, Karpov Institute of Physical Chemistry, Vorontsovo Pole 10, Moscow, Russia 105064

³ Department of Engineering Sciences, Uppsala University, Box 534, 751 21 Uppsala, Sweden

⁴ ESS, Tunavägen 24, 223 63 Lund, Sweden

⁵ Nuclear Physics Institute, Academy of Sciences of the Czech Republic, 25068 Rez, Czech Republic

⁶ Department of Chemistry and Chemical Engineering, Chalmers University of Technology, Göteborg 412 96, Sweden

⁷ Institut für Material- und Geowissenschaften, Technische Universität Darmstadt, Alarich-Weiss-Strasse 2, Darmstadt 64287, Germany

⁸ Institute of Solid State Chemistry, Ural Branch of the Russian Academy of Sciences, Ekaterinburg, Russia 620990

of the high-temperature ferromagnetic transition at about 195 K [2, 7]. The degree of the B'/B'' cationic ordering strongly affects the magnetic properties of these perovskites [8]. In the perfectly ordered monoclinic structure (s.g. $P2_1/n$), the B' and B'' cations are arranged alternately in the $2c$ and $2d$ Wyckoff positions. However, experimentally it has been found that, for many perovskites, the B' and B'' atoms get interchanged resulting in the formation of anti-site disorder [8]. The presence of anti-site disorder results in anti-ferromagnetic coupling due to super-exchange interactions between $\text{Ni}^{2+}\text{--O}^{2-}\text{--Ni}^{2+}$ and $\text{Mn}^{4+}\text{--O}^{2-}\text{--Mn}^{4+}$ ions, which causes magnetic frustration [2]. Another possible disorder can arise when the material crystallizes in the orthorhombic $Pnma$ structure, where, B' and B'' ions arrange randomly at the $4b$ site. In this case both Ni and Mn ions are present in 3+ valence states and nearest neighbour $\text{Ni}^{3+}(\text{Mn}^{3+})\text{--O--Ni}^{3+}(\text{Mn}^{3+})$ antiferromagnetic interactions occur along with $\text{Ni}^{3+}\text{--O--Mn}^{3+}$ ferromagnetic interactions.

The degree of anti-site disorder depends on various factors like cationic mismatch, the nature of B' and B'' ions and the synthesis conditions. The synthesis and annealing temperature, and time, are crucial for the degree of ordering [9, 10]. It is found that the anti-site disorder could originate from insufficient annealing time and local variation of concentration of B' and B'' cations. The aim of this investigation is to determine the crystallographic and magnetic structure of NNMO with definite Ni/Mn content in wide temperature ranges including T_C and investigate possible relationships between its structure and the physical properties.

2 Experimental

2.1 Sample preparation

The samples $\text{Nd}_2\text{NiMnO}_6$ were obtained by a solid-phase reaction method from the oxides Nd_2O_3 , NiO and Mn_2O_3 , all with purities greater than 99.95%. Stoichiometric mixtures of reagent-grade precursor materials were first weighted, thoroughly mixed and ball milled with a zirconia media for 4 h, then pressed under the pressure of 295 MPa, and sintering in air at 1223, 1373, 1523 and 1623 K for 12 h at each temperature with intermediate grinding after each heating step. This was followed by a series of grinding and sintering procedures until a pure diffraction pattern was obtained. This method yielded samples with a minimal quantity of NiO impurities. Presence of NiO or MnO are often found in the double perovskites A_2NiMnO_6 synthesized at high temperatures [5, 11, 12]. Upon the final annealing, the ceramic specimens were cooled inside the furnace to room temperature.

Additional post-synthesis annealing was also performed at 1273 K for 12 h in vacuum to study any change in the oxygen stoichiometry.

Several ceramic samples were synthesized using the above procedure. Phase pure, cation and oxygen stoichiometric (see below for chemical analysis) were selected for the studies subsequently described. However, as large amounts of materials were required for NPD studies (about 3 g of material), it was necessary to mix several samples; some with minor amounts of NiO. As a result, as seen in Fig. 5, it was necessary to consider few percents ($\leq 3\%$) of a secondary phase of NiO, in the refinements of the neutron data. A similar parasitic phase could be detected by XRPD on the sample used in the NPD studies.

2.2 Chemical composition

Phase purity and compositions of the obtained ceramics was analysed by X-ray powder diffraction (Bruker D8 with $\text{CuK}\alpha_1$ radiation) and energy-dispersive X-ray spectroscopy (EDS). A PANalytical Epsilon 3XLE EDXRF spectrometer was used to perform the measurements of cation composition of powder samples. Each powder sample was transferred into a sample cup assembled with a high transmission Prolene ($4\text{ }\mu\text{m}$) supporting foil. All analyses were conducted in a helium/air environment. The oxygen content in all samples was checked by iodometric titration.

2.3 X-ray photoelectron spectroscopy

X-ray photoelectron spectroscopy (XPS) was conducted using an Ulvac-Phi Quantera II spectrometer, which employs monochromatic $\text{AlK}\alpha$ radiation (1486.7 eV). For the present experiments the analysis spot was set to a diameter of 100 μm , and an electron take-off angle of 45° was used. The energy scale was calibrated against reference samples of Au, Ag and Cu, according to ISO 15472 standard [13]. Measurements were conducted on powdered samples of the perovskite, as well as on binary NiO (Baker, 99.9%), MnO_2 (Highways Ind. 99.9%) and Nd_2O_3 (Aldrich, 99.9%) reference samples. Powders were fastened on small pieces of carbon tape, attached to microscope slides, thus electrically floating the samples. Measurements were conducted under constant charge neutralization with an electron flood gun and low energy (10 eV) Ar^+ ions, as described in reference [2]. This procedure guarantees stable measurement conditions, but not an exact binding energy. Adventitious carbon was used as charge reference, and the position of the C 1s peak set to 284.8 eV. To remove some adsorbed surface contaminants (but not affect the sample), and increase the sample signal, a presputter step was employed using a 200 eV Ar^+ ionbeam for 12 s. Survey and core level spectra for all elements in the samples were collected.

2.4 Diffraction

The phase identification and purity of powder samples at 295 K was characterised from X-ray powder diffraction (XRPD) patterns obtained on a Bruker D8 Advance diffractometer (Lynx-Eye position-sensitive detector, CuK α radiation) in the 2θ range 10° – 152° with a step size of 0.02° . Diffraction patterns were also recorded at low temperatures using a Bruker D8 (Lynx-Eye position-sensitive detector, CuK α_1 radiation) from 20 K to room temperature. Additional temperature and magnetic-field dependent X-ray powder diffraction measurements were performed on a custom-built diffractometer in transmission geometry (MoK α radiation, 2θ range from 7° to 67° with a step size of 0.009°), which has been described in detail in [14]. NNMO powder was mixed with a NIST640d standard reference silicon for correction of geometric errors. Temperature in the range from 11 to 300 K was controlled by means of a custom SHI closed-cycle Helium cryofurnace. The cooling rate between the measurements was 2 K/min and the sample temperature was stabilized for 15 min before data collection. Measurements were performed for zero field cooling protocol and isothermally under fixed magnetic fields between 1 and 5 T.

To gain more information of the cation ordering and the oxygen position and occupancies neutron powder diffraction (NPD) was performed. The different neutron scattering lengths for Nd (7.69 fm), Ni (10.3 fm) and Mn (-3.73 fm) makes it possible to separate the cations with good precision. Furthermore, the scattering power of oxygen (5.803 fm) is comparable to the cations which also gives more structural information. For this, and the possibility of getting information of the magnetic structure, neutron diffraction patterns were collected at temperatures between 8 and 290 K at the MEREDIT diffractometer at the Nuclear Physics Institute, ASCR (Rez outside Prague, Czech Republic). The wavelength was set to 1.46 Å by a copper mosaic monochromator. Several grams of the powdered samples were inserted in a cylindrical vanadium container and the data were collected between 4° and 144° in 2θ with a step length of 0.08° .

2.5 Refinement of the crystal and magnetic structure

XRPD and NPD patterns were analyzed with the Rietveld method [15] implemented in the software FullProf [16]. The diffraction peaks were described by a pseudo-Voigt profile function. Peak asymmetry corrections were made for angles below 35° (2θ). Background intensities were estimated by interpolating between up to 40 selected points or described by a polynomial with six coefficients. During the refinements the metal cations (Nd, Ni and Mn) were allowed to vary their occupation on the possible metal sites. Refinement of the site occupancy was performed in monoclinic space group $P2_1/n$,

assuming as starting values at the $2c$ - and $2d$ -sites, a random distribution of the mixed transition metals, 50% Mn and 50% Ni. The occupancies obtained for the room-temperature patterns were kept constant while refining the magnetic data at low temperature. The IVTON software [17] was employed to characterize the coordination spheres of the A and B -site cations and to obtain bond lengths, volumes of coordination polyhedral and displacements of cations from the centers of the coordination polyhedra. The magnetic structure was refined as an independent phase in which only Ni/Mn cations were included. The magnetic propagation vector was determined from the peak positions of the magnetic diffraction peaks. Representational analysis to determine the symmetry allowed magnetic structures was performed using the softwares BasIreps (implemented in the FullProf Suite) and SARAh [18].

2.6 Magnetic measurements

The magnetic response as a function of temperature, $M(T)$, was measured using the zero-field cooling ($M_{ZFC}(T)$) and field cooling ($M_{FC}(T)$) protocols in the temperature range 10 K to 300 K using a small magnetic field, $H = 0.8$ kA/m (10 Oe). To investigate the high-field response and to estimate the magnetic entropy change a $M(T)$ measurement using an applied magnetic field of $H = 800$ kA/m (10 kOe) was also performed. The magnetic response as a function of applied magnetic field, $M(H)$, was investigated at 10 K in the field interval of $H = \pm 4000$ kA/m (± 50 kOe). All magnetometry measurements were performed using a Quantum Design MPMS SQUID magnetometer.

3 Results and discussion

The XRD patterns of Nd₂NiMnO₆, Fig. 1, may be indexed using either a monoclinic $P2_1/n$ or an orthorhombic $Pnma$ space group. To find the space group that best represents the NNMO phase, fits to both models are shown in Fig. 1. It was observed that the superstructure reflection at $Q \sim 1.4 \text{ \AA}^{-1}$ is better described from the monoclinic space group (Fig. S1 in the Supplementary Material), in agreement with previous reports; see References in Table 1. Unit cell parameters are also included for comparison. The variation of the lattice parameters and monoclinic angle in Table 1 is likely to stem from differences in the synthesis conditions (times, temperatures, atmospheres, etc). The structure has tilted NiO₆ and MnO₆-octahedra that are corner-sharing and stacked along the c direction in the monoclinic structure. Figure 1 shows a polyhedral linkage of the monoclinic double perovskite structure. The rare earth ions, Nd³⁺, are located between two consecutive layers. The structure is a typical rock salt arrangement for the octahedral sites. The cooperating tilting

of the NiO_6 and MnO_6 -octahedra with apparent distorted crystal structure can also be seen when compared to the cubic $Fm\bar{3}m$ -model. Although Rietveld refinement of the XRD patterns suggests a disordered alignment of $\text{Ni}^{2+}/\text{Mn}^{4+}$ in NNMO. However, a definite answer is not possible to obtain from XRD due to the similar scattering power of Ni and Mn.

Polyhedral analysis of the structure, characterizing the coordination spheres of the A and B cations including bond lengths and displacements of the cations from the centers of the coordination polyhedra were performed. The results of polyhedral analysis for Nd, Ni and Mn for NNMO are listed in Table 2. A quantitative estimate of the valence states of

the cations was obtained by calculating the bond valence sums (BVS). The results suggest a mixed $(2+/3+)$ valence state of Ni, and $4+$ for Mn. Nd^{3+} cation has a reduced coordination number, 9 instead of 12, which is a result of the movement of the anions due to octahedral tilting. Furthermore, the A-site Nd cations have shifted away significantly from the centre of its coordination polyhedra. Significant variation of the Nd–O distances, polyhedral volume and distortions were observed. The B-site cations are positioned in octahedral centers but variation in B–O distances is quite evident (Table 2 in Supporting Information).

EDS measurements establishes a nominal cation ratio rather close to $\text{Nd}:\text{Ni}:\text{Mn} = 2:1:1$. The Nd, Ni and Mn

Fig. 1 Refined XRD patterns of $\text{Nd}_2\text{NiMnO}_6$ using the models **a** $P2_1/n$ and **b** $Pnma$. To visualise the similarities and differences between the two models insets are shown for both models

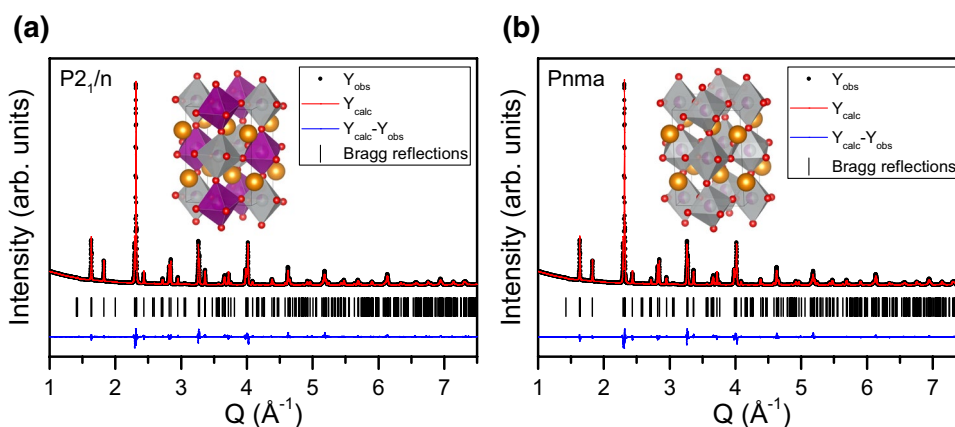


Table 1 Unit cell parameters for monoclinic (s.g. $P2_1/n$) $\text{Nd}_2\text{NiMnO}_6$ at room temperature, and ferromagnetic transition temperature (T_C)

a (Å)	b (Å)	c (Å)	β (°)	Method	(T_C) (K)	References
5.4097(1)	5.4844(1)	7.6691(2)	90.018(7)	XRPD	195*	This work
5.4097(3)	5.4798(3)	7.6635(4)	90.116(4)	NPD		This work
5.4150(5)	5.4882(4)	7.6770(6)	90.136(7)	XRPD	193	[19]
5.4160(2)	5.4706(3)	7.6701(4)	90.04	XRPD	196*	[20]
5.4194(1)	5.5004(1)	7.6825(1)	90.01	XRPD	193*	[5]
5.4024(9)	5.4768(9)	7.660(1)	90.00	NPD	200	[7]
5.514(1)	5.478(1)	7.777(2)	90.01	NPD	Not reported	[21]
5.4154(2)	5.4684(3)	7.6723(3)	90.06	XRPD	194	[22]
5.4162(2)	5.4963(5)	7.6718(1)	90.04	XRPD	192*	[6]
5.4142(1)	5.4633(1)	7.6690(1)	90.0207(1)	XRPD	200	[23]

*Indicates a significant anomaly in the magnetic data near 100 K. Standard deviations are given in the parenthesis

Table 2 Polyhedral analysis of $\text{Nd}_2\text{NiMnO}_6$ at 295 K

Cation	c.n	δ (Å)	ξ (Å)	V(Å ³)	Δ	Valence
Nd	9	0.35	2.581 ± 0.242	30.94(3)	0.097	2.97
Ni	6	0	2.003 ± 0.154	10.62(2)	0.009	2.77
Mn	6	0	1.943 ± 0.145	9.65(2)	0.014	4.15

(δ —Cation shift from centroid, ξ —Average bond distance and bond length limits, V—Polyhedral volume, Δ —Polyhedral volume distortion

compositions have been renormalized independently of oxygen. For a nominal $\text{Nd}_2\text{NiMnO}_6$ composition, the expected fraction of total cations are 0.5, 0.25 and 0.25 for Nd, Ni and Mn, respectively. In the as-synthesised sample the stoichiometry was determined to $\text{Nd} = 0.501(3)$, $\text{Ni} = 0.249(3)$ and $\text{Mn} = 0.250(3)$, whereas for the annealed sample $\text{Nd} = 0.498(3)$, $\text{Ni} = 0.249(3)$ and $\text{Mn} = 0.253(3)$. This is an indication that the additional annealing does not effect the oxygen composition in the compound. Scanning electron micrographs showed a uniform distribution of grains of sizes between 1.6 and 1.8 μm . The oxygen content was measured using iodometric titration and the measured value of oxygen was 5.986(13), consistent with thermogravimetric analysis (TGA). Additional characterization of the NNMO sample after annealing indicates no detectable change in composition or structure.

XPS survey spectra of the powder samples (not shown) show no other contaminations than adventitious carbon on the surface. XPS spectra of the Ni 2p, Mn 2p and Nd 3d core levels (top spectra in respective panel) are shown in Fig. 2, together with binary reference samples (bottom spectra in respective panel). The XPS Nd 3d core level spectrum from the NNMO sample exhibit the same peak shape and position as the Nd_2O_3 reference sample and matches literature for the same [24], thus showing that Nd is present in the 3+ state in NNMO. The NNMO sample shows distinct differences compared to the binary reference oxides, thus indicating that other oxidation states are present in the NNMO perovskite. There are, however, factors that contribute to uncertainties in the XPS measurements. Firstly, overlaps with Auger bands in the spectra from NNMO (Ni 2p and Mn LMM, as well as Mn 2p and Ni LMM) which will disturb the background and shape of the photoelectron peaks. Secondly, the presence of complex peak shapes and a shake-up satellite (in the Ni 2p region) also limits the precision of any peak fitting procedure. Comparing the present data with the reference samples, as well as with literature for different nickel [25, 26] and manganese oxides [27–29], it is clear that Ni is present in 2+ and 3+ states in the NNMO, and that the Mn is present 4+ and 3+ states. The presence of Mn^{2+} can be excluded due to the lack of shake-up satellite (+5 eV from $\text{Mn } 2p_{3/2}$) in the spectra [29]. Thus, it can be concluded that both Ni and Mn have mixed valences in the NNMO material. Similar mixed valences have been observed previously for NNMO by Singh et al. and Shi et al. [5, 30].

In Fig. 3a data for the low field ($H = 0.8 \text{ kA/m}$) $M_{\text{ZFC}}(T)$ and $M_{\text{FC}}(T)$ measurements are presented. A rapid increase of the magnetization as a function of temperature is observed below 200 K, reflecting the ferromagnetic interaction of the Ni/Mn ions along the $\text{Mn}^{4+}\text{--O--Ni}^{2+}$ bonds of the structure ($T_C \sim 195 \text{ K}$). The temperature-dependent magnetization shows two additional features, a weak inflection near 100 K (more evident in the ZFC data presented in

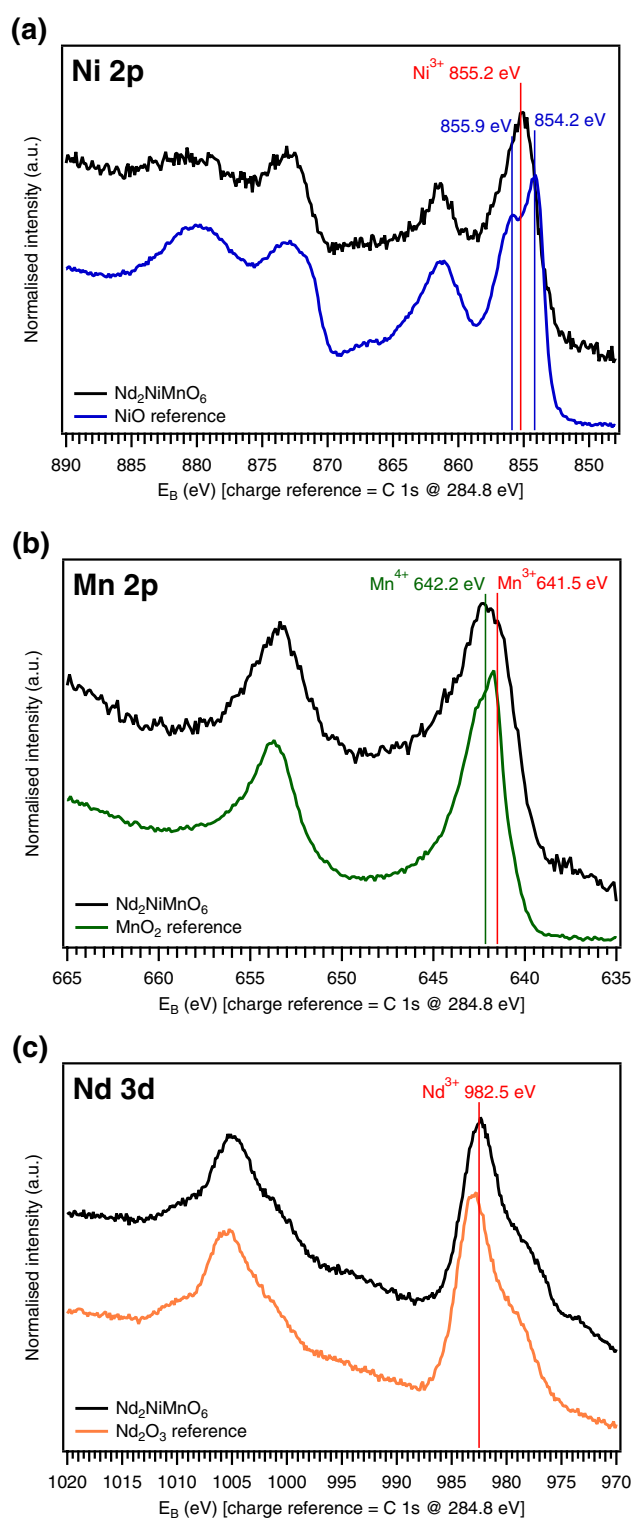


Fig. 2 XPS spectra from the NNMO perovskite and proper reference sample for the **a** Ni 2p spectra **b** Mn 2p spectra **c** and Ni 3d spectra

inset) and a downturn below 50 K. The low field behavior of the sample is similar to that reported previously [5–7, 31]. The sharpness and magnitude of the anomaly near

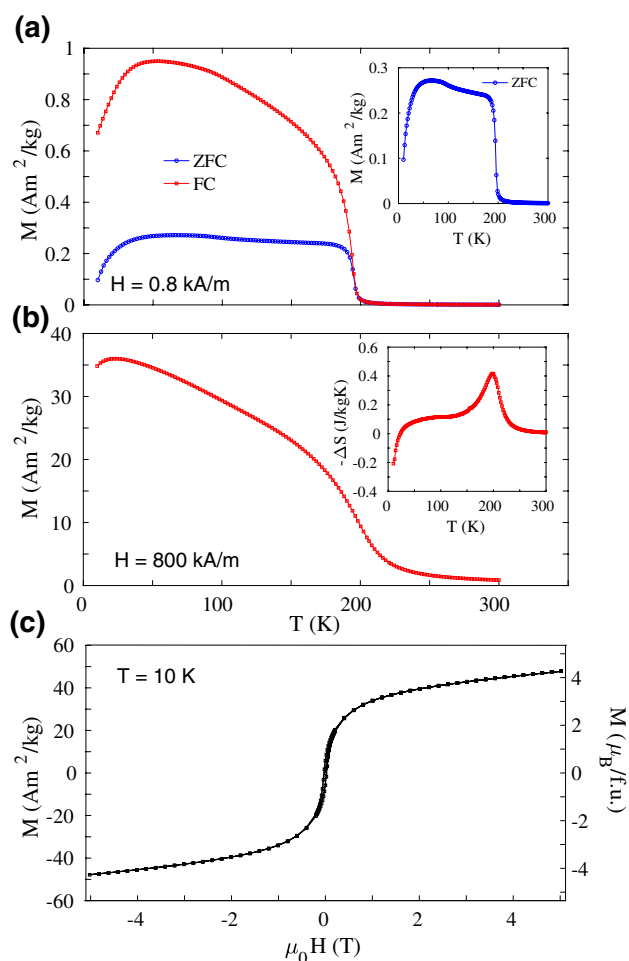


Fig. 3 Magnetisation (M) as a function of temperature and applied magnetic field. **a** ZFC and FC magnetization recorded in $H = 0.8 \text{ kA/m}$; the inset shows an enlargement of the ZFC curve in the region of the 100 K anomaly. **b** FC magnetization recorded in $H = 800 \text{ kA/m}$; the inset shows the variation of the magnetic entropy change estimated from the temperature derivative of the magnetization data (plotted as $-\Delta S$). **c** Magnetic field dependence of the magnetization at $T = 10 \text{ K}$; corresponding $\mu_B/\text{f.u.}$ values are indicated on the right axis

100 K possibly reflects the amount of antisite disorder ($\text{Mn}^{4+} - \text{O} - \text{Mn}^{4+}/\text{Ni}^{2+} - \text{O} - \text{Ni}^{2+}$ bonds) [5, 6]. The downturn of the magnetization below 50 K is on the other hand related to the $4f$ magnetic moments of the Nd^{3+} ions which are coupled antiferromagnetically to the $3d$ moments of Mn/Ni [7, 8]. Fig. 3b shows the high field ($H = 800 \text{ kA/m}$) $M(T)$ behavior. As observed earlier, the magnetization decreases at low temperatures, even in such relatively high fields [8]. Using the relation $\Delta S \sim dM/dT \times \mu_0 H$, the magnetic entropy change for $\mu_0 H = 1 \text{ T}$ was estimated from this data [32]. Around T_C , $-\Delta S \approx 0.4 \text{ J/kgK}$, while at 10 K, $-\Delta S \approx -0.2 \text{ J/kgK}$, inset of Fig. 3b. Magnetization as a function of applied magnetic field, $M(H)$, at 10 K is shown in Fig. 3c. The sample exhibits a small coercivity of about 22 kA/m at

this temperature. The magnetization of the sample does not saturate up to $\mu_0 H = 5 \text{ T}$, owing to the contribution of the Nd^{3+} moments, which are forced to turn away from their antiparallel alignment with the Mn/Ni ions at zero field to finally align with the field at very large magnetic fields [23]. M amounts to about $4.3 \mu_B/\text{f.u.}$ at 5 T, i.e. a much lower value than the $5 \mu_B/\text{f.u.}$ expected for perfectly ordered $\text{Mn}^{4+}/\text{Ni}^{2+}$ without antisite disorder and only paramagnetic Nd moments.

The recorded XRD patterns collected as a function of both temperature and applied magnetic field could, as well as the conventional diffraction pattern, Fig. 1, be refined in both the monoclinic and the orthorhombic settings. In the monoclinic setting, which is the preferred one from neutron diffraction, the monoclinic angle β is close to 90° , well in agreement with Table 1. The changes in the unit cell parameters a , b and c upon different temperatures and magnetic fields are summarized in Fig. 4. When no field is applied the unit cell decreases continuously with temperature. However, as seen in Fig. 4a, the lattice parameters change irregularly near (T_C), and, as seen in (b), a clear difference in the a and b unit cell parameters is observed at 100 K when applying a magnetic field; both increase significantly compared to the zero field values and reach saturated values at the employed field strengths ($>1 \text{ T}$). At the measured temperatures above and below 100 K no significant difference can be detected in the unit cell parameters, with respect to magnetic field.

The recorded neutron diffraction patterns were collected to resolve which space group NNMO belong to as well as to get more detailed information about the magnetic nature. In Fig. 5 the neutron diffraction patterns for 290 and 8 K are presented. The 290 K data supports the suggested phase from analysis of the XRPD patterns, i.e. the monoclinic space group $P2_1/n$ with unit cell parameters in agreement with those from XRPD but with a more pronounced monoclinic angle (90.12° compared to 90.02° from XRPD), Table 1. The space group $P2_1/n$ has two positions for the cations Ni and Mn where the majority of each position is occupied by respective ion. However, to fully describe the NPD patterns partial ordering with a 80/20% ratio of the metals is needed. BVS was calculated for the neutron diffraction data, and it was found that the B' -site, $2b$ ($1/2\ 0\ 0$), has a larger size ($2.018(1) \text{ \AA}$) which matches an occupation by 80% of Ni^{2+} and 20% of Mn^{3+} . The site B'' , $2c$ ($1/2\ 0\ 1/2$), is smaller ($1.926(1) \text{ \AA}$) which is occupied by 80% of Mn^{4+} and 20% of Ni^{3+} . The B' octahedron has short apical distances where the B'' octahedron is apically elongated. After cooling to low temperature, the intensity of reflections ($0\ 0\ 2$) and ($1\ \bar{1}\ \bar{1}$) increase (at $Q = 1.64 \text{ \AA}^{-1}$) due to the magnetic state of the compound, Fig. 5b. Several models generated from the representational analysis were tested and the best fit was obtained for I^3 with the propagation vector $\mathbf{k} = (0\ 0\ 0)$ and the magnetic moment aligned

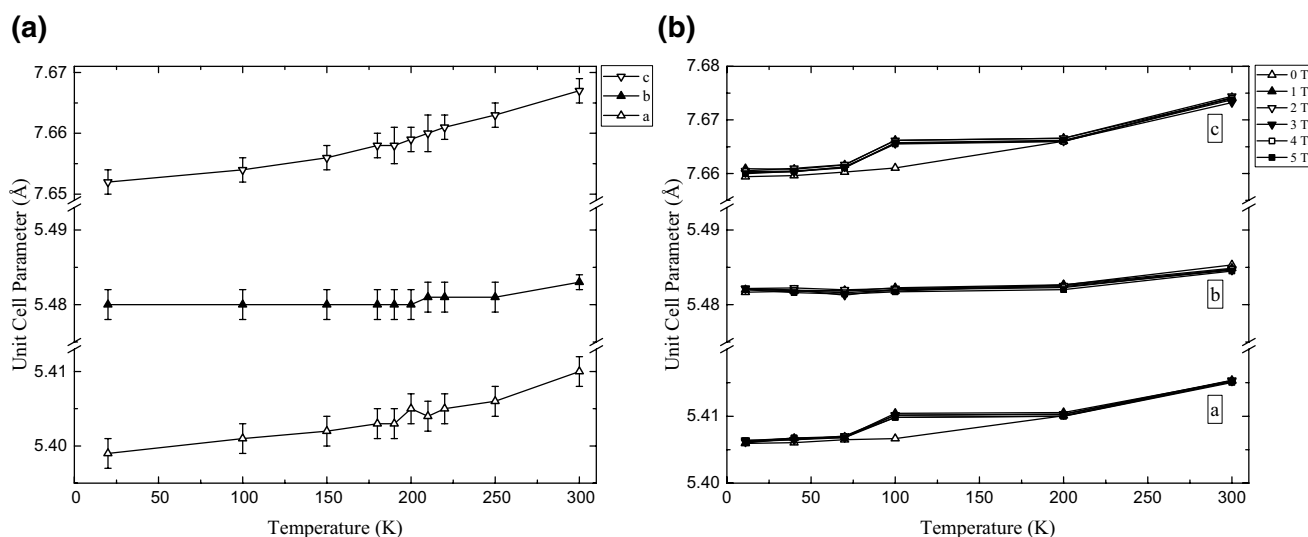


Fig. 4 Evolution of unit cell parameters as a function of **a** temperature and **b** applied magnetic field. The monoclinic angle β was found to be close to 90° in these refinements

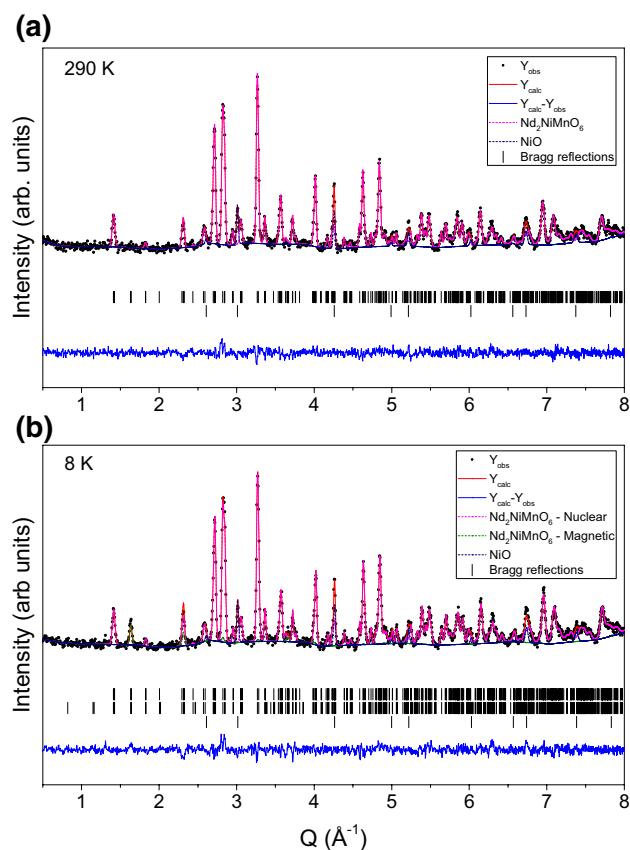


Fig. 5 **a** Neutron diffraction data at 290 K and **b** 8 K. The observed diffractions pattern as well as the result of the refined model are shown as well as the scattering from each individual phase

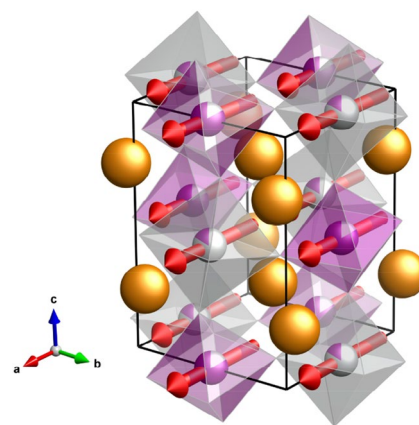


Fig. 6 Model of the magnetic structure of $\text{Nd}_2\text{NiMnO}_6$

along the crystallographic a -direction which is visualised in Fig. 6. The calculated magnetic moment at 8 K for the B' site (80% Ni^{2+} and 20% Mn^{3+}) is $2.1(1) \mu_B$ and for the B'' site (80% Mn^{4+} and 20% Ni^{3+}) is $1.9(1) \mu_B$. This model is different compared to previous reports which have suggested an alignment of the Ni and Mn ions along the crystallographic c -direction [7]. That magnetic structure model was also tested for the the diffraction data presented here. However, the reflections $(0\ 0\ 2)$ and $(1\ \bar{1}\ \bar{1})$, at $Q = 1.64 \text{\AA}^{-1}$, is then shifted to higher Q -values, giving an S-shape in the difference curve (also observed in the data in [7]). Therefore, the model with magnetic moments along the a -direction is concluded to best describe the neutron diffraction data. In the model presented by Sanchez-Benitez et al. [7] magnetic moments for Nd are also reported, however, the present

neutron data could be modelled considering solely the magnetic contribution of the *B*-site cations.

4 Conclusions

Phase pure, stoichiometric ceramic samples of the double perovskite $\text{Nd}_2\text{NiMnO}_6$ have been systematically studied with X-ray powder diffraction, XPS and magnetometry. Additionally, neutron powder diffraction was used on a larger sample batch with small NiO impurities. The cation ordering in the perovskite type compounds are driven by the difference in the ionic radii and charge of the octahedral cations. The similar ionic radii of Ni and Mn makes a disordered structure preferred, while possible valence states of the Ni and Mn can lead to an ordered structure in NNMO. The coexistence of both the ordered and disordered structures with different symmetries makes NNMO complicated magnetically. The structure was found to be monoclinic $P2_1/n$ with partial mixing on the *B* site with mixed valence states. The magnetic structure of the ferromagnetic state established below 195 K was determined. The magnetic moments are aligned ferromagnetically along the crystallographic *a*-direction.

Acknowledgements Open access funding provided by Uppsala University. Financial support for this work from the Russian Foundation for Basic Research (Grant 18-03-00245), the Swedish Research Council (VR), and the Swedish Foundation for Strategic Research, project “SSF Magnetic materials for green energy technology” is gratefully acknowledged. Measurements were carried out at the CANAM infrastructure of the NPI CAS Rez supported through MEYS Project No. LM2011019.

Open Access This article is distributed under the terms of the Creative Commons Attribution 4.0 International License (<http://creativecommons.org/licenses/by/4.0/>), which permits unrestricted use, distribution, and reproduction in any medium, provided you give appropriate credit to the original author(s) and the source, provide a link to the Creative Commons license, and indicate if changes were made.

References

1. J.Y. Moon, M.K. Kim, Y.J. Choi, N. Lee, *Sci. Rep.* **7**(1), 16099 (2017)
2. D. Choudhury, P. Mandal, R. Mathieu, A. Hazarika, S. Rajan, A. Sundaresan, U.V. Waghmare, R. Knut, O. Karis, P. Nordblad, D.D. Sarma, *Phys. Rev. Lett.* **108**, 127201 (2012)
3. N. Rogado, J. Li, A. Sleight, M. Subramanian, *Adv. Mater.* **17**(18), 2225 (2005)
4. M. Nasir, S. Kumar, N. Patra, D. Bhattacharya, S.N. Jha, D.R. Basaula, S. Bhatt, M. Khan, S.W. Liu, S. Biring, S. Sen, *ACS Appl. Electr. Mater.* **1**(1), 141 (2019)
5. C. Shi, Y. Hao, Z. Hu, *J. Phys. D* **44**(24), 245405 (2011)
6. R. Yadav, S. Elizabeth, *J. Appl. Phys.* **117**(5), 053902 (2015)
7. J. Sánchez-Benítez, M.J. Martínez-Lope, J.A. Alonso, J.L. García-Muñoz, *J. Phys.* **23**(22), 226001 (2011)
8. S. Pal, S. Govinda, M. Goyal, S. Mukherjee, B. Pal, R. Saha, A. Sundaresan, S. Jana, O. Karis, J.W. Freeland, D.D. Sarma, *Phys. Rev. B* **97**, 165137 (2018)
9. G. King, P.M. Woodward, *J. Mater. Chem.* **20**, 5785 (2010)
10. S. Vasala, M. Karppinen, *Prog. Solid State Chem.* **43**(1), 1 (2015)
11. X. Yuan, Q. Li, J. Hu, M. Xu, *Physica B* **424**, 73 (2013)
12. Y. Lin, X. Chen, X. Liu, *Solid State Commun.* **149**(19), 784 (2009)
13. M.P. Seah, *Surf. Interface Anal.* **31**(8), 721 (2001)
14. T. Faske, W. Donner, *J. Appl. Crystallogr.* **51**(3), 761 (2018)
15. H.M. Rietveld, *J. Appl. Crystallogr.* **2**(2), 65 (1969)
16. J. Rodríguez-Carvajal, *Physica B* **192**(1–2), 55 (1993)
17. T. Balić Žunić, I. Vicković, *J. Appl. Crystallogr.* **29**(3), 305 (1996)
18. A. Wills, *Physica B* **276–278**, 680 (2000)
19. A. Ali, Y. Sharma, Y. Singh, *AIP Conf. Proc.* **1953**(1), 040017 (2018)
20. A.K. Singh, S. Chauhan, S.K. Srivastava, R. Chandra, *Solid State Commun.* **242**, 74 (2016)
21. M. Mouallem-Bahout, T. Roisnel, F. Bourée, G. André, C. Moure, O. Peña, *Prog. Solid State Chem.* **35**(2), 257 (2007). International Conference on Perovskites at EMPA, 2005
22. W.Z. Yang, X.Q. Liu, H.J. Zhao, Y.Q. Lin, X.M. Chen, *J. Appl. Phys.* **112**(6), 064104 (2012)
23. S. Pal, S. Jana, S. Govinda, B. Pal, S. Mukherjee, S. Keshavarz, D. Thonig, Y. Kvashnin, M. Pereiro, R. Mathieu, P. Nordblad, J.W. Freeland, O. Eriksson, O. Karis, D.D. Sarma, *Phys. Rev. B* **100**(4), 045122 (2019)
24. J.P. Baltrus, M.J. Keller, *Surf. Sci. Spectra* **26**(1), 014001 (2019)
25. A.N. Mansour, *Surf. Sci. Spectra* **3**(3), 231 (1994)
26. A.N. Mansour, C.A. Melendres, *Surf. Sci. Spectra* **3**(3), 263 (1994)
27. M.A. Stranick, *Surf. Sci. Spectra* **6**(1), 31 (1999)
28. M.A. Stranick, *Surf. Sci. Spectra* **6**(1), 39 (1999)
29. A.J. Nelson, J.G. Reynolds, J.W. Roos, *J. Vac. Sci. Technol. A* **18**(4), 1072 (2000)
30. G. Singh, P. Singh, R. Choudhary, A. Dogra, *J. Alloys Compd.* **739**, 586 (2018)
31. R. Booth, R. Fillman, H. Whitaker, A. Nag, R. Tiwari, K. Ramanujachary, J. Gopalakrishnan, S. Lofland, *Mater. Res. Bull.* **44**(7), 1559 (2009)
32. S.A. Ivanov, M.S. Andersson, J. Cedervall, E. Lewin, M. Sahlberg, G.V. Bazuev, P. Nordblad, R. Mathieu, *J. Mater. Sci.* **29**(21), 18581 (2018)